ACS Catalysis

Research Article

pubs.acs.org/acscatalysis

Rationalizing Acid Zeolite Performance on the Nanoscale by Correlative Fluorescence and Electron Microscopy

Jordi Van Loon,[†] Kris P. F. Janssen,[‡] Thomas Franklin,[†] Alexey V. Kubarev,[†] Julian A. Steele,[†] Elke Debroye,[‡] Eric Breynaert,[†] Johan A. Martens,[†] and Maarten B. J. Roeffaers*[,†]

[†]Center for Surface Chemistry and Catalysis, Faculty of Bioscience Engineering, KU Leuven, 3001 Heverlee, Belgium

[‡]Department of Chemistry, Faculty of Sciences, KU Leuven, 3001 Heverlee, Belgium

Supporting Information

ABSTRACT: The performance of zeolites as solid acid catalysts is strongly influenced by the accessibility of active sites. However, synthetic zeolites typically grow as complex aggregates of small nanocrystallites rather than perfect single crystals. The structural complexity must therefore play a decisive role in zeolite catalyst applicability. Traditional tools for the characterization of heterogeneous catalysts are unable to directly relate nanometer-scale structural properties to the corresponding catalytic performance. In this work, an innovative correlative super-resolution fluorescence and scanning electron microscope is applied, and the appropriate analysis procedures are developed to investigate the effect of small-port H-mordenite (H-MOR) morphology on the catalytic performance, along with the effects of extensive acid leaching. These correlative measurements revealed catalytic activity at the interface between intergrown H-MOR crystallites that was assumed inaccessible, without compromising the shape selective properties. Furthermore, it was found that extensive acid leaching led to an etching of the originally accessible microporous structure, rather than the formation of an extended mesoporous structure. The associated transition of small-port to large-port H-MOR therefore did not render the full catalyst particle functional for catalysis. The applied characterization technique allows a straightforward investigation of the zeolite structure−activity relationship beyond the single-particle level. We conclude that such information will ultimately lead to an accurate understanding of the relationship between the bulk scale catalyst behavior and the nanoscale structural features, enabling a rationalization of catalyst design.

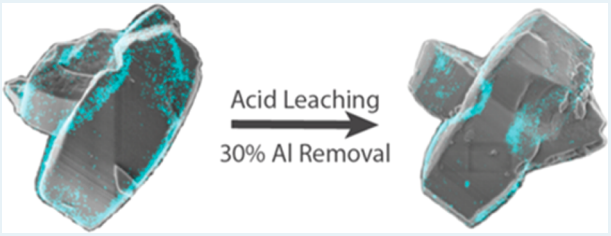

KEYWORDS: *zeolite catalysis, mordenite, dealumination, structure−activity relationship, super-resolution microscopy, single-molecule fluorescence microscopy, integrated fluorescence and electron microscope*

INTRODUCTION

Zeolites are widely used as solid acid catalysts in both laboratory-scale research and industrial chemical processes.[1−3] Their catalytic activity and chemoselectivity are strongly influenced by the accessibility of individual active sites that are located within the characteristic ordered microporous structure.[4] Structural imperfections such as defects and meso- and macropores are therefore believed to be key determinants of catalyst performance.[5,6] This is specifically true for zeolites with unidirectional pore systems, such as mordenites (MOR). The MOR framework consists of 12- and 8-membered ring channels running along the crystallographic *c* axis and a network of side pockets oriented along the *b* axis that are not effectively interconnecting the pores along the *c* axis.[7] Since molecular transport of most organic molecules can only occur through the 7.0 Å × 6.5 Å sized 12-membered ring (12MR) channels, the MOR framework porosity can be regarded as unidirectional. As a consequence, molecular diffusion is easily obstructed, and as-synthesized mordenite crystals therefore often display restricted mass transport.[8] According to the literature, this so-called small-port (SP) behavior is most probably caused by crystallographic stacking faults or extra-framework aluminum species deposited in the micropores.[7,9−11] The obstructed molecular accessibility in the micropores of such small-port mordenites (SP-MORs) limits the catalytic activity to pore entrances located near the outer surface of the crystals.[8] These mass transport constraints are typically circumvented by applying postsynthetic dealumination, such as acid leaching or hydrothermal treatments, to introduce mesopores into the structure.

In this work, a newly developed integrated fluorescence and electron microscope (iFlEM) is applied to investigate the effect of SP-MOR nanocrystallite structure on the catalytic performance. The novelty of this research is 2-fold. First, we describe the development of a new tool that for the first time enables catalyst structure to be linked to its performance on the nanoscale. The main advantages of using such an integrated instrument instead of independent microscopes are the strongly

Received: April 7, 2017
Revised: June 6, 2017
Published: June 22, 2017

DOI: 10.1021/acscatal.7b01148
ACS Catal. 2017, 7, 5234−5242

reduced risk of sample contamination and that, after an initial alignment of the system, structural images and catalytic activity maps are conveniently overlaid. The second novelty is that, in contrast to idealized, micrometer-large crystals, which have been used before, this work employed a commonly applied industrial zeolite batch, containing a large amount of complex intergrown particles.

The latter is of importance since most synthetic zeolite batches, including mordenites, do not consist of perfect uniform crystals, but rather a wide range of particle morphologies is present. It often follows that zeolite particles exhibit complex intergrowths and obvious structural defects.[11,12] The influence of this structural complexity on the catalytic performance or postsynthetic dealumination is not yet understood at the relevant length scales, mainly because traditional analytical methods used in zeolite and catalysis research are unable to directly link the effects of structural imperfections to the impact on the catalytic performance.[4,5,12,13] Particularly for zeolites with a one-dimensional porous structure, pore blocking has a tremendous effect on catalyst performance, but this has so far not been directly related to the local catalyst structure.[14] For example, electron microscopy enables the investigation of structural details down to the atomic scale.[15] However, a direct correlation of this structurally resolved information to the catalytic performance, which is typically measured on the bulk scale, cannot be made due to the intrinsically large inter- and intraparticle heterogeneity. At best, the outcome of ensemble averaged catalyst testing can lead to generalized insights on the interplay between catalyst structure and activity.

Fluorescence microscopy has undeniably proven its ability to characterize and visualize the catalytic performance down to the level of individual catalytic conversions.[16,17] More specifically, the optical transparency of zeolites enables the catalytic performance to be mapped out on the nanoscale through Nanometer Accuracy by Stochastic Chemical reActions, or NASCA.[18−20] The interpretation of these spatially resolved performance maps depends on morphological features that can typically be resolved from corresponding optical transmission images of the same catalyst particle. This approach is therefore limited to micrometer-sized crystals with well recognizable morphologies and structures. For example, fluorescence microscopy investigations have led to the elucidation of the impact of intergrowth structures within large H-ZSM-5 crystals on pore accessibility, chemical mobility, and catalytic performance.[19,21,22] Alternatively, a number of uniform nanometer-sized metal catalyst particles has been investigated.[8,23−25] These spatially resolved studies have so far demonstrated the impact of inter- and intraparticle heterogeneities on the overall catalytic performance.[26] Together, these investigations only focused on either large, perfect crystals or relatively small particles that are assumed to be uniform in size and morphology. However, this is not representative for actual industrially employed catalyst powders containing nonuniform nanoparticles and complex aggregates of nanocrystallites. Therefore, it is essential to correlate the nanoscale activity maps recorded by NASCA microscopy to structural information on the same particle on the same length scale.[16]

Detailed structure−activity relationships at the level of individual zeolite catalyst particles were recently obtained by the Weckhuysen group by combining transmission electron microscopy (TEM) with diffraction-limited confocal laser scanning fluorescence microscopy.[27,28] While very powerful, these static experiments are focused on investigating prestained samples and do not enable super-resolution imaging of the catalytic activity on the nanoscale. Furthermore, care has to be taken not to compromise the local catalyst structure during the sample slicing prior to the experiment. Chen and co-workers alternatively employed correlative fluorescence microscopy and scanning electron microscopy (SEM) to link catalytic activity to the structure of metal nanoparticles.[24,29,30]

This brief summary of earlier efforts to investigate the catalyst structure−activity relationship down to the nanoscale illustrates the relevance of developing an iFlEM approach as applied in the reported work. By linking nanoscale catalyst performance and structure, we uncover the significance of crystal intergrowths that induce extra-framework porosity and their role on catalyst performance before and after acid leaching. Furthermore, it was discovered that there is no significant mesopore creation through extensive acid leaching, demonstrating the need for an additional hydrothermal treatment in order to truly circumvent the small-port behavior of MOR zeolites.

EXPERIMENTAL METHODS

Integrated Fluorescence and Electron Microscope. The iFlEM setup consists of an inverted epifluorescence wide-field microscope integrated into an SEM (FEI Quanta 250 FEG), by means of a customized chamber door (SECOM, Delmic BV; Figure 1).[31,32] On the outside of the sample chamber, a 532 nm diode pump solid state laser (Omicron laserage) is directed through the chamber window by means of a 442/532 nm dichroic mirror with accompanying excitation

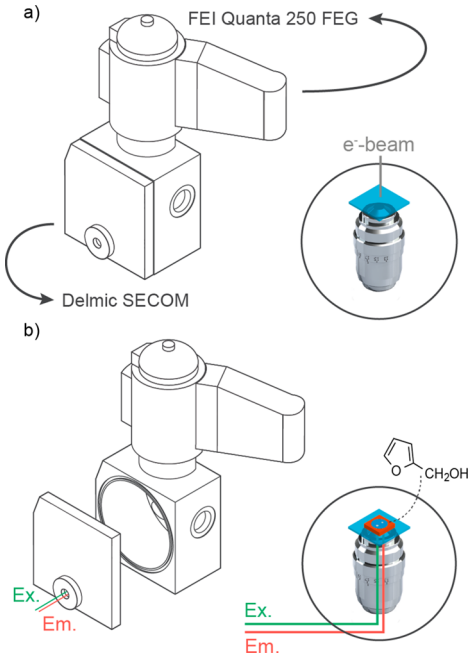

Figure 1. Schematic representation of the iFlEM showing the chamber window that is fitted into the customized SEM chamber door and is essential to the presented approach. The design is based on the SECOM platform (Delmic B.V.). Both subimages also show an inside view of the electron beam/sample/objective lens configuration in the situation that (a) a structural image is being acquired with SEM and (b) the single turnover precise catalytic activity map is obtained after bringing the sample to atmospheric pressure, attaching a perfusion chamber to the cover slide, and adding the reagent solution.

DOI: 10.1021/acscatal.7b01148
ACS Catal. 2017, 7, 5234−5242

filter (Figure 1b). A 100 × 1.4 NA CFI plan APO VC oil objective lens (Nikon) located inside the vacuum chamber provides the wide field excitation of the sample. As such, this system provides 1.9 kW cm^{-2} of excitation light on the sample. To operate the system under vacuum conditions (approximately 1 × 10^{-4} Pa), 1-ethyl-3-methylimidazolium acetate is applied as immersion liquid. The generated fluorescence is guided through the optically transparent window and passes through the dichroic mirror and a 542 nm LP emission filter, followed by a 2.5× camera lens in front of the EMCCD camera (Hamamatsu C9100-23B). The optically transparent chamber window is key to the functioning of the integrated system as it allows fluorescence and excitation light to travel through the chamber door. Hence, after venting the system, catalytic activity mapping can be started immediately. The described configuration provides a 32.8 × 32.8 μm^2 field of view and a 64 × 64 nm^2 pixel size on the investigated sample. Wide-field fluorescence movies were acquired with 30 ms exposure time. The linear polarized light experiments are performed after introducing a Glan-Thompson polarizer (Thorlabs) into the optical pathway before the dichroic mirror. A detailed schematic representation of the iFlEM is provided in the Supporting Information (Scheme S1).

Sample Preparation. The SP-MOR sample was obtained from Tosoh Corporation (HSZ-620HOA, Si/Al ratio: 7.5). Two droplets of a 10 mg/mL mordenite in Milli Q water suspension were spin-coated onto single-molecule clean cover slides at 3000 rpm for 60 s. These single-molecule clean 22 × 22 #1 cover slides were prepared by calcination for over 24 h in a static air oven at 450 °C, followed by a 1 h ozone treatment in a UV reactor (Ultraviolet products, PR-100). The spin-coated samples were additionally calcined in a static air oven at 450 °C to remove any impurities that could lead to residual fluorescence in the zeolite sample. To ensure that no structural changes were induced in the sample, a stepwise heating scheme was used (heating ramp of 1 °C/min and a 1 h dwell time at 80 and 150 °C; at 450 °C the temperature was held for at least 48 h).

Correlated Data Acquisition. The correlated NASCA experiments were always performed in a similar fashion. The prepared cover slide was attached onto a metal plate sample holder and mounted into the iFlEM. SEM images of the crystals were taken (2 kV, SE, high vacuum mode; Figure 1a), after which the sample chamber of the SEM was vented to atmospheric pressure and the chamber door was opened (Figure 1b). Next, a perfusion chamber (PC8R-1.0-CoverWell, Grace Bio laboratories) was attached onto the cover slide, and 50 μL of an 18 wt % FFA (Sigma-Aldrich, 98%, purified through vacuum distillation prior to use) solution in Milli Q water was added with a micropipette. Through a set of experiments with varying concentrations, this amount was established as the optimal concentration. The addition of FFA as the fluorogenic reagent leads to the formation of oligomeric reaction products, by means of the acid-catalyzed condensation reaction that is catalyzed on the Brønsted acid sites of the zeolite (Scheme S2).[17] These oligomers are composed of a conjugated backbone structure that provides the fluorescent properties to enable their observation in fluorescence experiments with single-molecule sensitivity.[19] In the NASCA experiment conducted on the acid leached sample, a reduced 8 wt % FFA in Milli Q water solution was added to ensure the single-molecule sensitivity for this catalytically more active sample. For our experiments, only crystals that show little or no background fluorescence were used.

NASCA Analysis. By fitting the point spread function of single emitters with a two-dimensional Gaussian function, their exact location is determined. The localizer software used to perform this analysis on the recorded fluorescence movies and produce the quantitative activity maps is available online (https://bitbucket.org/pdedecker/localizer) as a plugin for both Igor Pro (Wavemetrics) and Matlab (MathWorks).[33] The resolution achieved by this approach is approximately 20 nm.[19] Single fluorescent product molecules reappearing in consecutive frames before photobleaching were counted as one catalytic event. The software has a built-in consolidation functionality that finds reappearing molecules within a certain distance, allowing a certain blinking time. For these specific experiments, a respective distance of 50 nm and blinking time of 90 ms were employed. All the parameters mentioned above were obtained after a careful evaluation of different combinations of the different parameters. The quantitative NASCA images that result from this analysis are obtained by binning the data into 50 × 50 nm^2 areas. By additionally considering the imaging depth as a measure for the thickness of every voxel, i.e., 500 nm, the corresponding catalytic activity is obtained, which is represented by assigning a color scale to the resulting activity map.

The Overlay Procedure. The correlated micrographs shown in Figures 2, 3, and 4 were created using the image registration tool available in ImageJ. By selecting the same two reference points on both the qualitative activity map (produced using the localizer software) and the electron micrograph, the correct magnification, rotation and translation is obtained that is needed to accurately overlay both images. By merging the resized qualitative activity map and the electron micrograph with the merge channels command, the correlated micrograph is obtained. The cyan colored dots displayed on the SEM micrographs in this work represent the position where at least one turnover has taken place.

Molecular Size Calculation. The molecular diameters of FFA and pyridine were calculated using MarvinSketch (version 15.9.21.0), developed by ChemAxon.

Reaction-Pore Confinement Analysis. The Matlab analysis procedure that has been developed to perform the reaction-pore confinement analysis is available online (https://drive.google.com/open?id=0ByLzCpEAweEkbTdHQlI-xeUlzRkE). In this analysis, the NASCA image data obtained from analyzing the respective linear polarized light experiments, using the localizer software and binning them into 200 × 200 nm^2 zones, are used as input. The two separate data sets are carefully screened for drift using a built-in drift check function. The reaction-pore confinement plot in Figure 3e has been drift corrected for +64 nm along the y axis. No drift correction was needed to obtain the reaction-pore confinement plot of the HNO_3 leached sample. A second parameter is set as the lower limit (LL). As such, any bins in the image only composed of fluorescent background molecules are filtered out. The LL for the analysis of the performed experiments is set to five turnovers. Finally, an upper threshold is set for the transparency range that qualitatively displays the number of turnovers detected within the respective bins. The threshold is set at 10% of the maximal bin value obtained by summing the turnovers of both linear polarized light experiments in every bin.

Acid Leaching. Dealumination has been achieved by refluxing 1 g of the SP-MOR zeolite sample at 90 °C for 8 h

DOI: 10.1021/acscatal.7b01148
ACS Catal. 2017, 7, 5234−5242

using 20 mL of a 1 M HNO_3 (Sigma-Aldrich, 65%) in Milli Q solution while vigorously stirring the slurry. The acid leached zeolite was separated from the acidic solution by means of Büchner-filtration using warm distilled water until the permeate obtained a neutral pH. Finally, the zeolite was dried in a static air oven for 24 h at 85 °C.

Bulk Scale Characterization. Elemental analysis of the HNO_3 leached sample has been performed using ICP-OES (Varian 720-ES). N_2-adsorption isotherms have been obtained at −196 °C (Micromeritics 3Flex 3400 physisorption instrument). The reference and HNO_3 treated samples have been degassed prior to the experiment for 4 h at 250 °C under vacuum conditions (1 Pa). The specific surface area has been obtained by BET analysis. ^{27}Al spectra were acquired on a Bruker 500 MHz spectrometer, spinning the sample at 10 kHz at the magic angle. The spectra were recorded using a one pulse sequence with $\pi/12$ pulses of 2.90 μs using a recycle delay of 0.8 s and referenced to a solution of 0.5 M $Al(NO_3)_3$ dissolved in 0.5 M HNO_3. Each spectrum was acquired with 1024 scans using a spectral width of 19 607 Hz recorded with a 2048 point FID size and processed with a 5 Hz apodization.

Bulk Scale Reactivity Testing. The bulk scale naphthalene isopropylation reaction was performed in the liquid phase using a high-pressure 15 mL TOP reactor for 8 h at 200 °C and under 2×10^6 Pa of N_2 gas (99.999%). A figure of the apparatus was added to the Supporting Information (Figure S1). The reaction mixture consisted of 1.84 mmol of naphthalene (Sigma-Aldrich, ≥99%), 4 mmol of 2-propanol (Biosolve ≥99.8%), 9 mL of cyclohexane (Sigma-Aldrich, ≥ 99.8%), and 100 mg of the MOR catalyst. The catalyst powder is used as provided by the manufacturer or as obtained after acid leaching, i.e., crystal size 1−3 μm and average particle size 18 μm. After 8 h of reaction, the reactor was cooled by placing it in an ice bath. The reaction mixture was analyzed using a gas chromatograph (Shimadzu, CP-Sil 8, FID detector) in split injection mode (split ratio 20) using N_2 carrier gas. After injection, the temperature was programmed as follows: 5 min hold at 40 °C, heating to 280 °C at 4 °C/min, and finally a 10 min holding time. A total of 2 mmol of n-tetradecane (TCI, ≥ 99%) was added as an internal standard for quantitative gas chromatography (GC) analysis. Identification of the compounds was carried out using gas chromatography−mass spectrometry.

Pyridine Staining. Prior to pyridine adsorption, the mordenite sample is dropcasted and calcined as described in the sample preparation paragraph. After calcination, the cover slides, which are contained in glass vials, are cooled down to approximately 280 °C. At this point, two droplets of pyridine (Sigma-Aldrich, ≥ 99%) are pipetted onto the bottom of the vial, the glass vial is closed using its lid, and the sample is left for several hours for the adsorption to take place.

Raman Experiments. The Raman experiments were performed using a Zeiss 100× 1.3 NA oil immersion objective lens and a Coherent argon-ion gas laser, tuned to operate at 488 nm. This resulted in a spot size of approximately 460 nm and a spatial resolution of approximately 230 nm, used to probe intergrown particles at discrete locations. The microprobe power density used was 15 kW cm^{-2}, which is well below the damage threshold limit. The relative amount of pyridine adsorbed at the different positions in the different samples is quantified by determining the ratio of the pyridine to mordenite band intensity from the Raman spectra.

RESULTS AND DISCUSSION

When the iFlEM approach is used, detailed electron micrographs of the H-MOR catalyst particle at study are collected from the top of the sample and linked to catalytic activity maps of the same catalyst particle obtained from the bottom side of the sample (Figure 1). The latter is achieved by measuring single catalytic turnovers using the fluorescence microscope after addition of an aqueous furfuryl alcohol (FFA) solution. Localization and accumulation of the individual fluorescent reaction products results in nanoscale activity maps.[17,19] Figure 2a shows a typical scanning electron micrograph of an intergrown crystal in an industrial H-MOR batch, which mainly contains aggregated SP-MOR crystals. The corresponding schematic representation is presented in Figure 2b. The different MOR crystals that make up the aggregate are pseudocolored as a guide for the eye and to simplify the later discussion. Here, the small blue H-MOR crystal protrudes from the larger orange crystal, and on the opposite side a large defect is present. Judging from the shape of the defect, it likely results from another intergrown crystallite that has broken off. After this detailed morphological characterization, FFA was added to the SP-MOR cluster, enabling the visualization of single acid-catalyzed turnovers by recording the fluorescent FFA oligomer formation. The individual fluorescent reaction products were subsequently localized with nanometer precision and their locations (cyan dots) overlaid with the high-resolution SEM image, as shown in Figure 2c. Since the optical focus was centered around the middle of the aggregate, the recorded catalytic events originate from an optical slice around the center of the aggregate of approximately 500 nm thickness (Scheme S1). This is also apparent from the location of the recorded catalytic events with respect to the scanning electron micrograph.

The majority of the observed catalytic events are clustered in a zone about 300 nm wide, delineating the outer surface of the aggregated particle. This is indicative of small port behavior as the size of the FFA reagent molecule should enable diffusion through the 12MR channels (molecular diameter is about 6.1 Å), and earlier research on MFI type zeolites with a characteristic 10MR microporous structure has additionally revealed full accessibility.[8,17,34] Importantly, experiments in this work are performed shortly after the addition of FFA, and during this period the catalytic activity remains constant. The observed small-port behavior is therefore assumed to be an effect of mass transport limitations rather than pore blocking, which might gradually occur by accumulation of oligomers. In the latter case, the catalytic activity would decrease during the experiment. Second, varying numbers of turnovers are observed within the active zone. The small port behavior becomes even clearer when looking at the NASCA image obtained in Figure 2d by binning the measured catalytic turnovers into 50 × 50 nm^2 zones, which yields a quantitative view on the matter. In the main crystal (orange), most of the acid-catalyzed oligomerization reactions are limited to two opposite crystal facets. On the basis of the crystallographic structure, in combination with the morphology of the crystals, these slightly curved and roughened facets are identified as the crystallographic (001) facets where the 12MR pores are surfacing.[8,35] This observation shows that catalytic conversions in SP-MOR are limited to the acid sites available in the first few hundred nanometers behind the 12MR pore mouths. At the other facets, the microporous zeolite framework, and, hence, the catalytically

DOI: 10.1021/acscatal.7b01148
ACS Catal. 2017, 7, 5234−5242

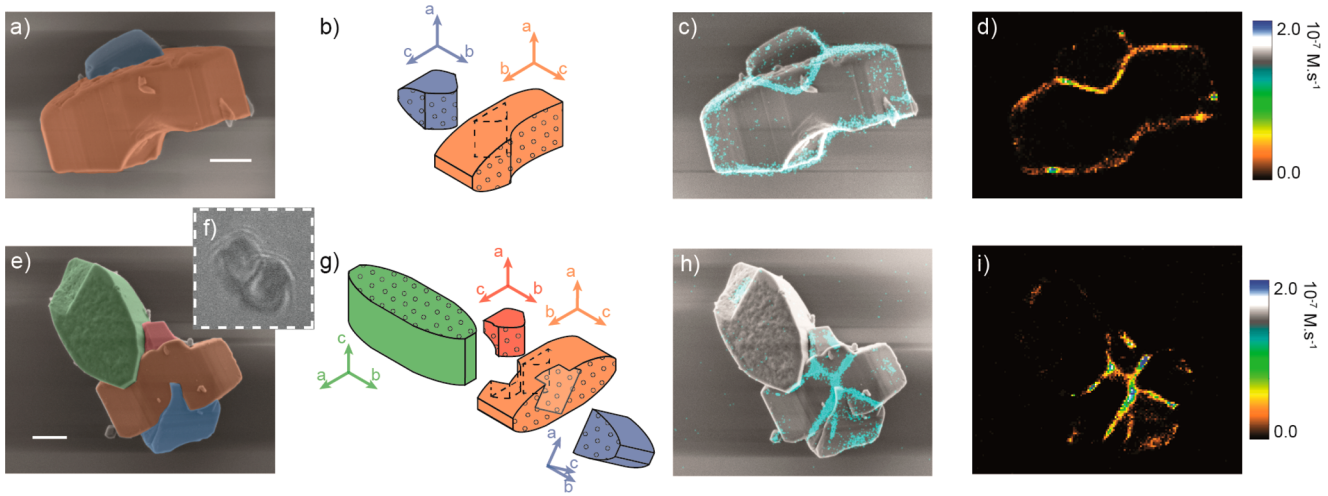

Figure 2. Images recorded using the iFlEM of two intergrown SP-MOR particles. (a, e) Pseudocolored scanning electron micrographs of intergrown crystallites and (b, g) the corresponding schematic representations indicating the different crystallographic axes. The (001) facets, where the 12MR channels surface, are marked by the dotted pattern indicating the 12MR pore entrances (for the original images, see Figures S2 and S3). (c, h) Overlay images of the detected individual fluorescent products (cyan dots) on the scanning electron micrographs, referred to as correlative micrographs and (d, i) the quantitative NASCA images obtained by binning the turnovers in 50 × 50 nm^2 zones. (f) Optical transmission image of the second aggregate. Scale bars: 1 μm.

active sites, are not accessible toward the FFA substrate. Note that the sparse turnovers detected at these facets can be related to acid sites at the outer surface or minute crystal imperfections. Surprisingly, also a significant number of catalytic turnovers is observed away from the outer surface and inside the main crystal, in the zone underneath the intergrown crystal at the top. The width of this catalytically active zone is comparable to that at the (001) facets at the crystal exterior. Judging from the shape of this catalytically active area, it can be assigned to the interface between the intergrown crystals, i.e., the highly defective area between the blue and orange crystals. Note that the activity of this region is similar to that observed at the readily accessible (001) facets and that no activity gradient is observed from the outside of the crystal toward the most deeply buried part of the intergrowth. It can therefore be concluded that the extra-framework porosity at this interface is sufficient to allow reagent molecules to readily reach the active sites along the intergrowth.

Figure 2e and f display the scanning electron micrograph and optical transmission image of another SP-MOR aggregate in this industrial H-MOR batch. A direct comparison clearly demonstrates that the structural complexity of small particles in typical zeolite samples cannot be captured by diffraction limited optical imaging. From the scanning electron micrograph, the structural details of this aggregate can be resolved, with the corresponding schematic representation shown in Figure 2g. The crystal at the top part (green) is a nearly complete crystal with an obvious defect at the top. Again, from the shape of the defect, it seems to have resulted from a broken off intergrown crystallite. Judging from the morphology of the particle (*vide supra*), the 12MR micropores run perpendicular to the rough (001) top facet along the optical z axis. In the center of the aggregate, another large crystal (orange) is present, perpendicular to the top (green) crystal. The 12MR pores in this crystal run parallel to the imaging plane, connecting the curved (001) facets where two more protruding crystals (red and blue) are present. The slightly different orientation of these two protruding crystals suggests that both are independent of each other.

Similar to the first aggregate (Figures 2a–d), the catalytic reactivity of this particle was measured by adding the fluorogenic FFA reagent solution and subsequently localizing the individual catalytic turnovers. Figure 2h shows the positions of localized individual catalytic events overlaid with the corresponding electron micrograph. The corresponding NASCA image is shown in Figure 2i. The interface of the central crystal (orange) with the intergrown crystals (red and blue) results in a highly active x-shaped zone of activity. Additionally, significant catalytic activity is observed at the interface between the central (orange) and top (green) crystals. The width of the catalytically active zones, measuring about 300 nm, and the absence of an activity gradient within this zone is in line with earlier observations on the first aggregate. The absence of catalytic activity in the upper (green) crystal can be explained by the orientation of the crystal; the 12MR micropores run parallel to the propagation direction of the excitation light (optical z axis). As the fluorescent product molecules are spatially constrained within the microporous structure, the molecules will be aligned along the micropore orientation. This results in a minimal overlap between the electric field vector of the excitation light and the transition dipole moment of the fluorescent product molecules.[8,36]

Clearly, the absence of a perfect coalignment between the crystal lattices of the intergrown crystals results in a local discontinuity of the zeolite framework at the boundary between these SP-MOR crystals. The resulting extra-framework porosity facilitates molecular diffusion and leads to an enhanced molecular accessibility. As such, this results in a zone of high catalytic activity at the interface between the individual crystallites, away from the outer surface. The catalytic activity at these intergrowths accounts for respectively 28 and 67% of the total catalytic activity observed in the two examples. These data clearly underline the importance of intergrowths on the overall performance of these H-MOR zeolites. At the same time, these results, showing activity away from the outer surface, also indicate that an aluminum gradient cannot be the origin of the observed activity profile, i.e., active crystallite edges and inactive crystallite center. On the other hand, it cannot be

DOI: 10.1021/acscatal.7b01148
ACS Catal. 2017, 7, 5234–5242

deduced from these observations whether this catalytic activity is only linked to acid sites within the SP-MOR micropores or if some portion of the activity is linked to defect sites at the highly defected interface. This is important, since the latter would have a negative impact on the shape selectivity.[37,38] Whereas product molecules formed within the confinement of the microporous structure are expected to be aligned along the 12MR pore direction, molecules formed on active sites directly located on the highly accessible intergrowth boundary should not show any preferential orientation.[8,36] Hence, the orientation of the fluorescent product molecules with respect to the one-dimensional porous structure is a good indicator of the pore confinement, which is crucial for shape selectivity. The orientation of fluorescent reaction products can be straightforwardly visualized by implementing linear polarized excitation light.[36]

To quantitatively investigate the pore confinement of individual fluorescent reaction products, an aggregate of three intergrown crystals from the same SP-MOR batch was examined in Figure 3. In this cluster, the 12MR pores of the respective crystals are oriented almost perpendicular to each other. The aggregate itself was oriented in such a way that the 12MR pores of the individual crystals are along the optical *x*, *y*, and *z* axes. When excitation with circular polarized light is performed (Figure 3a), fluorescent oligomers oriented in the *xy* plane are detected. A schematic representation of the cluster in which the different axes are assigned is given in Figure 3b. As observed in Figure 2c and h, catalytic activity is limited to zones of about 300 nm thickness starting from the 12MR pore mouths at the (001) facets and around the intergrowth interfaces. Note that the catalytically active zone along the interface between the middle (green) and left (orange) crystals is broader than the previously observed 300 nm (Figure 2c and h). As the catalytic activity map is a 2D projection of single turnovers taking place within a 500-nm-thick optical slice (*vide supra*), the width of the projection will depend on the relative orientation of the intergrowth structure to the optical section. Clearly, this interface does not follow any of the crystallographic axes of the other two intergrown crystals.

The introduction of a Glan−Thompson polarizer into the excitation pathway of the iFlEM polarizes the excitation light and allows its rotation over 360° in the optical *xy* plane. Next, we quantitatively investigate the polarization dependence by specifically employing two perpendicular polarization directions: first along the optical *x* axis, parallel to the 12MR pores of the orange crystal (Figure 3c), and, second, along the optical *y* axis, parallel to the 12MR pores in the blue crystal (Figure 3d). This investigation reveals that the formed fluorescent product molecules at the (001) facets of the respective crystals are mostly confined to their respective 12MR pores. When the excitation polarization is oriented along the direction of the 12MR pores of the orange crystal (i.e., the optical *x* axis), the number of catalytic turnovers observed in the blue crystal reduces drastically compared to the situation in which circular polarization was employed. Even though the catalytic reaction still occurs, the fluorescent product molecules are no longer efficiently excited, as the polarization direction of the excitation light is perpendicular to the orientation of the molecular excitation transition dipole moment. On the other hand, the opposite effect is observed when the polarization plane is oriented parallel to the optical *y* axis (Figure 3d). In this case, the blue crystal exhibits the majority of the catalytic activity, and only a fraction remains excitable and detectable in the

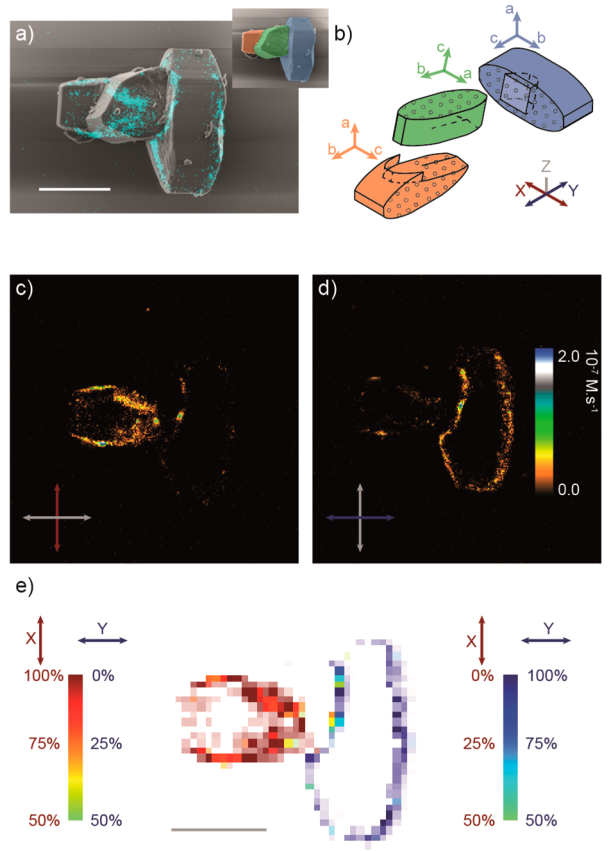

Figure 3. (a) Correlative structure−activity micrograph of a cluster of three intergrown crystallites obtained with circular polarized excitation light (for the original SEM image see Figure S4) and (b) the respective schematic representation with corresponding crystallographic and optical axes. Pore mouths of the 12MR are marked by the dotted pattern. The corresponding quantitative activity maps (accumulated activity recorded in 50 × 50 nm^2 project zones) are obtained with linear polarized excitation light along the one-dimensional porous structure in (c) the left (orange) crystal, i.e., the optical *x* axis, and (d) the right (blue) crystal, i.e., the optical *y* axis; the polarization direction is indicated by the highlighted optical axis. (e) The reaction-pore confinement plot obtained by combining the information from c and d, and after binning into 200 × 200 nm^2 areas. Scale bars: 3 μm.

orange crystal. Surprisingly, the same observation holds for the fluorescent product molecules formed at the intergrowth regions of the two crystals with the middle green crystal. As the 12MR pores of the latter crystal are oriented along the optical *z* axis, no significant contribution to the catalytic activity map is expected from the molecules confined within the microporous structure. Therefore, this is direct proof of the pore-confinement of reaction products near crystalline defects such as intergrowth interfaces.

Combining the information from Figure 3c and d into one reaction-pore confinement plot shows the local orientation of product molecules with respect to the 12MR pores: red-to-green and blue-to-green color scales are indicative of a transition from a situation in which all fluorescent product molecules are confined within the 12MR pores in the orange and blue crystals, respectively, to a situation where there is no preferential orientation (green; Figure 3e). The color intensity of each pixel provides a qualitative indication of the relative number of turnovers occurring in this zone. The reaction-pore confinement plot resulting from the aggregate in Figure 3

DOI: 10.1021/acscatal.7b01148
ACS Catal. 2017, 7, 5234−5242

mainly shows red and blue zones, corresponding to a confinement of approximately 86% over the whole particle. This value is obtained by determining the ratio of the number of fluorescent product molecules oriented along the local microporous structure, to the total number of catalytic turnovers observed over the catalyst particle. As such, this number represents the shape selectivity of the individual catalyst particle based on the FFA probe reaction.

The reaction-pore confinement determined during this experiment reveals that active sites are predominantly confined within the microporous structure as reaction products are preferentially oriented along the one-dimensional 12MR pores. However, catalytic activity is observed on all intergrowth structures, regardless of the crystallographic facets that are included. The formation of the crystallographic surface is therefore assumed to be incomplete where intergrowth formation has taken place. This leads to an opening up of the microporous structure. Additionally, active sites accessible through intergrowth structures are as reactive as those accessible through the intrinsic pore mouths on the (001) facets. This is an indication that mass transport inside intergrowths is unrestricted. As such, intergrowth structures are regarded as microporous voids that facilitate mass transport toward catalytically active sites located within the opened up crystallographic framework.

One method commonly applied to enhance molecular transport in SP-MOR catalysts is acid leaching, removing both framework and extra-framework aluminum species hindering molecular transport along the 12MR pores. Already in 1983, Raatz et al. reported that selective leaching of about 20% of the total aluminum content converts SP-MOR into the large-port form.[10] Since then, such postsynthetic treatments have become routine practice in H-MOR catalytic research.[39] The sample under investigation in this study was submitted to acid leaching by refluxing the SP-MOR zeolite sample in a HNO_3 solution.[40] Typically, the effect of this procedure on the zeolite and its catalytic performance is investigated by means of bulk-scale analysis, such as atomic spectroscopy to determine the bulk Si/Al ratio, or solid state nuclear magnetic resonance (NMR) to discriminate between framework (Al^{IV}) and extra-framework aluminum (Al^{VI}). Here, bulk analysis using inductively coupled plasma optical emission spectrometry (ICP-OES) revealed that about 30% of the aluminum was removed from the zeolite sample, and ^{27}Al NMR data additionally showed a slight preference toward extra-framework Al^{VI} removal. N_2-physisorption revealed a small increase in micropore- and external surface area. Finally, also a bulk scale naphthalene isopropylation reaction was performed on the mordenite catalysts. As such, the reactivity trends and shape selectivity properties, observed at the single particle level, before and after acid leaching, could be validated using an industrially relevant bulk scale process. The naphthalene isopropylation reaction revealed an increased activity from <1% conversion to 8% after HNO_3 leaching, indicating that the SP-MOR sample indeed became more active toward the alkylation of bulky organic molecules after the acid treatment. A summary of these bulk scale experiments can be consulted in the Supporting Information.

A combination of the newly developed iFlEM approach with the analysis tools introduced above provides a novel way to investigate the effects of acid leaching beyond the bulk scale. Figure 4 reveals the reaction-pore confinement for an HNO_3 treated aggregate consisting of three orthogonally intergrown

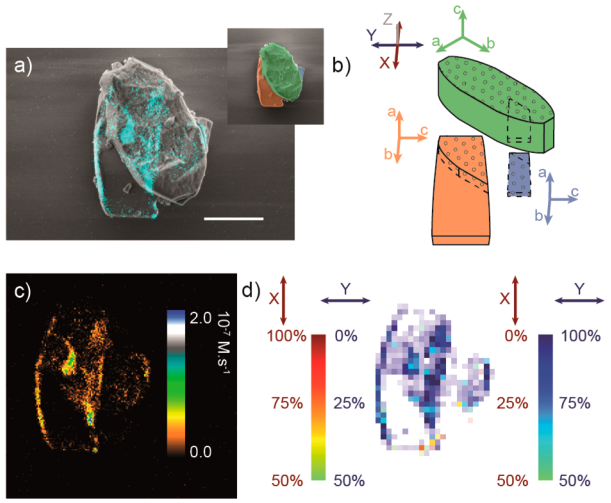

Figure 4. (a) Correlative structure–activity micrograph of three intergrown crystallites treated with HNO_3 obtained with circular polarized excitation light (for the original SEM image, see Figure S5) and (b) the respective schematic representation. The (001) facets, where the 12MR channels surface, are marked by the dotted pattern. (c) The corresponding quantitative activity map is obtained by using a 60% reduced fluorogenic reagent concentration compared to the previous experiments, and the recorded activity is accumulated in 50 × 50 nm^2 zones. (d) The molecular confinement plot is recorded by combining the information from the linear polarized excitation experiments as introduced in Figure 3e and after rebinning into 200 × 200 nm^2 areas. Scale bar: 2 μm.

crystals. The orange crystal is oriented with its 12MR pores running along the optical *y* axis, and the 12MR pores in the green crystal run parallel to the optical *z* axis. Additionally, a smaller crystallite (blue) is intergrown with the green crystal.

The correlated micrograph and quantitative activity map in Figure 4a and c show that the catalytic activity in the acid leached particle still predominantly resides at the edges of the orange crystal and the intergrowth, between the orange and green crystals. Furthermore, there is a zone of moderate catalytic activity in the green crystal which is attributed to the small intergrown blue crystal. As it is located beneath the green crystal, both the morphology of this crystal and the exact orientation of the intergrowth remain unresolved by means of SEM imaging. However, based on the information obtained from the reaction-pore confinement plot (Figure 4d), it is fair to assume that the orientation of the blue crystal is similar to that of the larger orange crystal. Note that the fluorogenic reagent concentration was reduced because of the increased reactivity over the untreated H-MOR sample (Figure S7). This increased reactivity is in line with the results from the bulk scale naphthalene isopropylation reaction. Additionally, the reaction-pore confinement plot in Figure 4d only reveals a slightly reduced molecular confinement of 83%. These results further confirm the earlier assumption that the formation of intercrystalline intergrowths led to locally enhanced access to the microporous structure. The effect of the acid treatment would otherwise be much more effective if intergrowths existed of combined micro-, meso-, and macroporous regions.

The presented nanoscale structure–activity experiments are a representative subset of a larger number of experiments (n = 10) and reveal that the location of the catalytic activity in H-MOR zeolites is not dramatically influenced by typical acid leaching. In earlier research, Liu et al. demonstrated that severe

DOI: 10.1021/acscatal.7b01148
ACS Catal. 2017, 7, 5234–5242

dealumination, removing more than 50% of the framework aluminum, was necessary to render the full catalyst particles accessible.[8] In their work, dealumination was achieved by means of a combined hydrothermal and acid treatment. Where acid leaching mainly enhances the local reactivity by etching the easily accessible microporous structure, the hydrothermal treatment introduces extensive meso- and macoporous defects that render the full catalyst particle accessible.

Intergrowth structures are affected to the same extent as the intrinsically active edges of the crystals, despite the former being much more defected. Even though over 30% of the aluminum has been removed, the H-MOR still displayed the typical reaction distribution and shape selective properties associated with small-port behavior, and therefore no transition from small-port to large-port H-MOR seemed to have taken place. Small- or large-port behavior is typically revealed by performing static benzene uptake experiments;[9,10] pyridine adsorption has been investigated using Raman spectroscopy to mimic such static experiments and confirms our findings based on the FFA oligomerization reaction. This approach involves the investigation of pyridine uptake before and after acid leaching in targeted areas of an intergrown particle: the crystallite edge, center, and on the interparticle intergrowth. The results are shown in the Supporting Information (Figure S8 and Table S4).

The pyridine uptake experiments indeed show an opening up of the microporous network and thus a transition of small-port to large-port H-MOR, even though pyridine is a bulkier molecule than the FFA reagent (molecular diameter for pyridine is about 6.7 Å). This significantly increased pyridine uptake in all three selected areas of the acid leached particle seems to contradict the outcome of the NASCA experiments. The discrepancy between both experiments can be explained by the dynamic aspect of the NASCA experiments in which molecular transport also plays a significant role. On the contrary, the pyridine distribution is determined after reaching equilibrium. Hence, we believe that the fluorogenic reaction gives a more accurate picture of the catalytically relevant domains. Alternatively, the presented observations could be interpreted as being an effect of Al zoning; however, this effect has not been reported for the MOR sample.[8]

CONCLUSIONS

In conclusion, the catalytic performance of acid zeolite nanocrystallites was studied by linking the catalytic performance, as observed in super-resolution fluorescence microscopy, to structural features of the same crystallite recorded by scanning electron microscopy. This enabled, for the first time, a direct observation of the effect of defects and intergrowths, commonly present in powdered zeolite batches, on the overall performance. First, intercrystalline intergrowth structures in SP-MOR aggregates were demonstrated to have a major contribution to the overall activity. The molecular confinement plots revealed that reaction products at the defect-rich intergrowth boundary preferentially align with the 12MR pores rather than taking random orientations. Hence, catalytically active sites at intergrowths are mainly located within the microporous structure. The intergrowth structure is therefore identified as a void space that allows unrestricted mass transport, enabling reactions to occur in the adjacent micropores. Second, dealumination by acid leaching mainly affects the intergrowths and the crystal edges. Surprisingly, even though more than 30% of aluminum was removed, and pyridine adsorption experiments showed a transition from small-port to large-port H-MOR, the reactivity pattern was not altered. Furthermore, a similar reaction-pore-confinement is observed on the crystal edges and intergrowths, before and after acid leaching, indicating the importance of such intergrowths for the overall catalyst performance. This is relevant information with the aim of rationalizing catalyst synthesis. Full catalytic utilization of the zeolite material on the other hand requires more severe postsynthetic treatments, e.g., more extensive acid leaching or a combination with hydrothermal treatment.[8,36,41] Future research should focus on the role of intercrystalline intergrowth structures with respect to catalyst coking and mesopore creation through hydrothermal treatment. Additionally, this line of research would benefit from the development of an *in situ* liquid cell that enables truly integrated experiments, allowing the fluorogenic reaction to be conducted within the vacuum of the SEM chamber.

ASSOCIATED CONTENT

Supporting Information

The Supporting Information is available free of charge on the ACS Publications website at DOI: 10.1021/acscatal.7b01148.

A scheme describing the NASCA technique, showing the optical slice and depicting the details of the iFlEM setup, a picture of the apparatus used for the bulk characterization, the raw SEM images of the different experiments, the bulk characterization data of untreated and acid leached samples, the results of an experiment on the untreated sample using the decreased FFA concentration, transmission images of intergrown particles before and after acid leaching loaded with pyridine indicating the areas probed with Raman, and the results of the pyridine uptake experiments (PDF)

AUTHOR INFORMATION

Corresponding Author

*E-mail: maarten.roeffaers@kuleuven.be.

ORCID

Eric Breynaert: 0000-0003-3499-0455

Maarten B. J. Roeffaers: 0000-0001-6582-6514

Author Contributions

The manuscript was written through contributions of all authors. All authors have given approval to the final version of the manuscript.

Notes

The authors declare no competing financial interest.

ACKNOWLEDGMENTS

The authors acknowledge financial support from the Research Foundation-Flanders (FWO, grant nos. G.0962.13, and G.0197.11, postdoctoral fellowship to E.D. and K.P.F.J.), KU Leuven Research Fund (C14/15/053, OT/12/059), the Hercules foundation (HER/11/14), and the Belgian Federal Science Policy Office (IAP-VII/05). The research leading to these results has received funding from the European Research Council under the European Union's Seventh Framework Programme (FP/2007-2013)/ERC Grant Agreement no. [307523], ERC-Stg LIGHT to M.B.J.R.

DOI: 10.1021/acscatal.7b01148
ACS Catal. 2017, 7, 5234−5242

REFERENCES

(1) Climent, M. J.; Corma, A.; Iborra, S. In *Zeolites and Catalysis: Synthesis, Reactions and Applications*, 1st ed.; Cejka, J., Corma, A., Zones, S., Eds.; Wiley-VCH: Weinheim, 2010.
(2) Dumesic, J. A.; Huber, G. W.; Boudart, M. In *Handbook of Heterogeneous Catalysis*, 2nd ed.; Ertl, G., Knözinger, H., Schuth, F., Weitkamp, J., Eds.; Wiley-VCH: Weinheim, 2008.
(3) Hagen, J. In *Industrial Catalysis: A Practical Approach*, 2nd ed.; Hagen, J., Ed.; Wiley-VCH: Weinheim, 2006.
(4) De Cremer, G.; Sels, B. F.; De Vos, D. E.; Hofkens, J.; Roeffaers, M. B. J. *Chem. Soc. Rev.* **2010**, *39*, 4703−4717.
(5) Janssen, K. P. F.; De Cremer, G.; Neely, R. K.; Kubarev, A. V.; Van Loon, J.; Martens, J. A.; De Vos, D. E.; Roeffaers, M. B. J.; Hofkens, J. *Chem. Soc. Rev.* **2014**, *43*, 990−1006.
(6) Rolison, D. R. *Science* **2003**, *299*, 1698−1701.
(7) Meier, W. M. *Z. Kristallogr. - New Cryst. Struct.* **1961**, *115*, 439−450.
(8) Liu, K. L.; Kubarev, A. V.; Van Loon, J.; Uji-I, H.; De Vos, D. E.; Hofkens, J.; Roeffaers, M. B. J. *ACS Nano* **2014**, *8*, 12650−12659.
(9) Freund, E.; Marcilly, C.; Raatz, F. *J. Chem. Soc., Chem. Commun.* **1982**, 309−310.
(10) Raatz, F.; Marcilly, C.; Freund, E. *Zeolites* **1985**, *5*, 329−333.
(11) van Geem, P. C.; Scholle, K. F. M. G. J.; van der Velden, G. P. M.; Veeman, W. S. *J. Phys. Chem.* **1988**, *92*, 1585−1589.
(12) Buurmans, I. L. C.; Weckhuysen, B. M. *Nat. Chem.* **2012**, *4*, 873−886.
(13) Weckhuysen, B. M. *Chem. Soc. Rev.* **2010**, *39*, 4557−4559.
(14) Magnoux, P.; Cartraud, P.; Mignard, S.; Guisnet, M. *J. Catal.* **1987**, *106*, 242−250.
(15) Lu, J.; Roeffaers, M. B. J.; Bartholomeeusen, E.; Sels, B. F.; Schryvers, D. *Microsc. Microanal.* **2014**, *20*, 42−49.
(16) Roeffaers, M. B. J.; De Cremer, G.; Uji-i, H.; Sels, B. F.; Jacobs, P. A.; De Schryver, F. C.; De Vos, D. E.; Hofkens, J.; Muls, B. *Proc. Natl. Acad. Sci. U. S. A.* **2007**, *104*, 12603−12609.
(17) Roeffaers, M. B. J.; Sels, B. F.; Uji-i, H.; Blanpain, B.; L'hoëst, P.; Jacobs, P. A.; De Schryver, F. C.; Hofkens, J.; De Vos, D. E. *Angew. Chem., Int. Ed.* **2007**, *46*, 1706−1709.
(18) Roeffaers, M. B. J.; Sels, B. F.; Uji-I, H.; De Schryver, F. C.; Jacobs, P. A.; De Vos, D. E.; Hofkens, J. *Nature* **2006**, *439*, 572−575.
(19) Roeffaers, M. B. J.; De Cremer, G.; Libeert, J.; Ameloot, R.; Dedecker, P.; Bons, A. J.; Bückins, M.; Martens, J. A.; Sels, B. F.; De Vos, D. E.; Hofkens, J. *Angew. Chem., Int. Ed.* **2009**, *48*, 9285−9289.
(20) Xu, W.; Kong, J. S.; Yeh, Y.-T. E.; Chen, P. *Nat. Mater.* **2008**, *7*, 992−996.
(21) Karwacki, L.; Stavitski, E.; Kox, M. H. F.; Kornatowski, J.; Weckhuysen, B. M. *Angew. Chem., Int. Ed.* **2007**, *46*, 7228−7231.
(22) Tachikawa, T.; Yamashita, S.; Majima, T. *J. Am. Chem. Soc.* **2011**, *133*, 7197−7204.
(23) Ristanović, Z.; Kerssens, M. M.; Kubarev, A. V.; Hendriks, F. C.; Dedecker, P.; Hofkens, J.; Roeffaers, M. B. J.; Weckhuysen, B. M. *Angew. Chem., Int. Ed.* **2015**, *54*, 1836−1840.
(24) Zhou, X.; Choudhary, E.; Andoy, N. M.; Zou, N.; Chen, P. *ACS Catal.* **2013**, *3*, 1448−1453.
(25) Han, K. S.; Liu, G.; Zhou, X.; Medina, R. E.; Chen, P. *Nano Lett.* **2012**, *12*, 1253−1259.
(26) Plessers, E.; Stassen, I.; Sree, S. P.; Janssen, K. P. F.; Yuan, H.; Martens, J.; Hofkens, J.; De Vos, D.; Roeffaers, M. B. J. *ACS Catal.* **2015**, *5*, 6690−6695.
(27) Karreman, M. A.; Buurmans, I. L. C.; Geus, J. W.; Agronskaia, A. V.; Ruiz-Martínez, J.; Gerritsen, H. C.; Weckhuysen, B. M. *Angew. Chem., Int. Ed.* **2012**, *51*, 1428−1431.
(28) Karreman, M. A.; Buurmans, I. L. C.; Agronskaia, A. V.; Geus, J. W.; Gerritsen, H. C.; Weckhuysen, B. M. *Chem. - Eur. J.* **2013**, *19*, 3846−3859.
(29) Sambur, J. B.; Chen, T.-Y.; Choudhary, E.; Chen, G.; Nissen, E. J.; Thomas, E. M.; Zou, N.; Chen, P. *Nature* **2016**, *530*, 77−80.
(30) Andoy, N. M.; Zhou, X.; Choudhary, E.; Shen, H.; Liu, G.; Chen, P. *J. Am. Chem. Soc.* **2013**, *135*, 1845−1852.
(31) Liv, N.; Zonnevylle, A. C.; Narvaez, A. C.; Effting, A. P. J.; Voorneveld, P. W.; Lucas, M. S.; Hardwick, J. C.; Wepf, R. A.; Kruit, P.; Hoogenboom, J. P. *PLoS One* **2013**, *8*, 1−9.
(32) de Boer, P.; Hoogenboom, J. P.; Giepmans, B. N. G. *Nat. Methods* **2015**, *12*, 503−513.
(33) Dedecker, P.; Duwé, S.; Neely, R. K.; Zhang, J. *J. Biomed. Opt.* **2012**, *17*, 126008.
(34) Roeffaers, M. B. J.; Ameloot, R.; Bons, A. J.; Mortier, W.; De Cremer, G.; De Kloe, R.; Hofkens, J.; De Vos, D. E.; Sels, B. F. *J. Am. Chem. Soc.* **2008**, *130*, 13516−13517.
(35) Simoncic, P.; Armbruster, T. *Am. Mineral.* **2004**, *89*, 421−431.
(36) Kubarev, A. V.; Janssen, K. P. F.; Roeffaers, M. B. J. *ChemCatChem* **2015**, *7*, 3646−3650.
(37) Csicsery, S. M. *Zeolites* **1984**, *4*, 202−213.
(38) Song, C. *Surf. Chem. Catal.* **2000**, *3*, 477−496.
(39) van Donk, S.; Janssen, A. H.; Bitter, J. H.; de Jong, K. P. *Catal. Rev.: Sci. Eng.* **2003**, *45*, 297−319.
(40) Giudici, R.; Kouwenhoven, H. W.; Prins, R. *Appl. Catal., A* **2000**, *203*, 101−110.
(41) Nesterenko, N. S.; Thibault-Starzyk, F.; Montouillout, V.; Yuschenko, V. V.; Fernandez, C.; Gilson, J. P.; Fajula, F.; Ivanova, I. I. *Microporous Mesoporous Mater.* **2004**, *71*, 157−166.

DOI: 10.1021/acscatal.7b01148
ACS Catal. 2017, 7, 5234−5242